g factor of topological interface states in $Pb_{1-x}Sn_xSe$ quantum wells

Jiashu Wang, Xinyu Liu, Tianyi Wang, Mykhaylo Ozerov, and Badih A. Assaf

g-factor of topological interface states in $Pb_{1-x}Sn_xSe$ quantum wells

Jiashu Wang,[1] Xinyu Liu,[1] Tianyi Wang[1], Mykhaylo Ozerov,[2] Badih A. Assaf[1]

[1] Department of Physics and Astronomy, University of Notre Dame, Notre Dame IN 46556, USA

[2] National High Magnetic Fields Laboratory, Florida State University, Tallahassee, FL, 32310, USA

Abstract: Topological crystalline insulators from the $Pb_{1-x}Sn_xSe$ family host textbook Dirac surface states that are nearly electron-hole symmetric and isotropic in momentum space. The high mobility of charge carriers possible in these materials, allow one to reach the quantum limit at reasonably achievable magnetic fields. We exploit this advantage to combine magnetooptical Landau level spectroscopy, Shubnikov-de Haas transport measurement and consistent modelling of the two experiments to precisely extract the band parameters of the topological states of this system along with their g-factor. We find an enhanced g-factor with field dependence compared with bulk states. This information is vital to the realization and understanding of novel quantized Hall effect stemming from the mirror protected valley-degenerate Dirac states of this material family.

Introduction:

Topological crystalline insulators (TCIs) are a class of topological matter, in which crystalline symmetry combines with time-reversal symmetry to ensure the existence of gapless surface states. IV-VI materials, including $Pb_{1-x}Sn_xSe$ and $Pb_{1-x}Sn_xTe$, have been identified as TCIs. [1–3] They have a simple rock-salt structure and host four Dirac cones along the [111] surface. This valley degeneracy can lead to novel quantum phenomena such as a quantum anomalous Hall effect with high Chern number and an interaction-induced quantum Hall nematic state. [4–6]

The electronic properties of bulk $Pb_{1-x}Sn_xSe$ have been explored by various techniques, such as magneto-transport [7–9], magneto-optics [10,11] and ARPES [3,12]. Magnetotransport has been commonly used to study the IV-VI materials, as the TCI properties can be reflected by the weak anti-localization effect and Shubnikov-de Haas oscillations [13,14]. However, most transport measurements fail to produce a complete electronic structure of the surface states, mostly due to the contribution from the bulk conducting channels. Extracting the g-factor and Zeeman splitting is particularly challenging without independent knowledge of where the Fermi level is and an independent indexing of the quantum oscillations. Notably, the g-factor of the surface states of TCIs has not yet been measured. There have been attempts to extract it using scanning tunneling spectroscopy measurements and quantum oscillations in Bi-based TIs. Values as high as 50 were recovered from the behavior of the N=0 Landau level in $Bi_2(Te,Se)_3$ [15], while quantum oscillations yielded inconsistent results [16–19]. This inconsistency is not an uncommon

issue, as the g-factor is known to be field and energy dependent for systems with non-parabolic dispersions resulting from strong spin-orbit interactions. [20]

In our previous work [13], we have successfully grown $Pb_{0.7}Sn_{0.3}Se$ quantum wells with high mobility and low carrier density. We studied their quantum coherent transport at low magnetic field. In this work, we perform high-field magnetotransport and magnetooptical measurements on the quantum wells to extract consistent band information valuable to realize and understand the quantum Hall effects predicted in this material system [4,21]. These parameters include the g-factor. We observed non-periodic quantum oscillations in the magnetoresistivity between 3T and 16T which are difficult to interpret without other experimental input. By employing magnetooptical Landau level spectroscopy, we extract the band parameters and model the Landau level dispersion versus magnetic field which allows us to reliably index observed oscillations. We find an excellent agreement between magnetotransport and magneto-optical measurement for a specific value of spin splitting. The crossing of Landau levels with the Fermi level allows us to model the quantum oscillations and extract the hole g-factor of the topological interface states of $Pb_{0.7}Sn_{0.3}Se$ quantum wells.

Experiment:

A. Sample structure
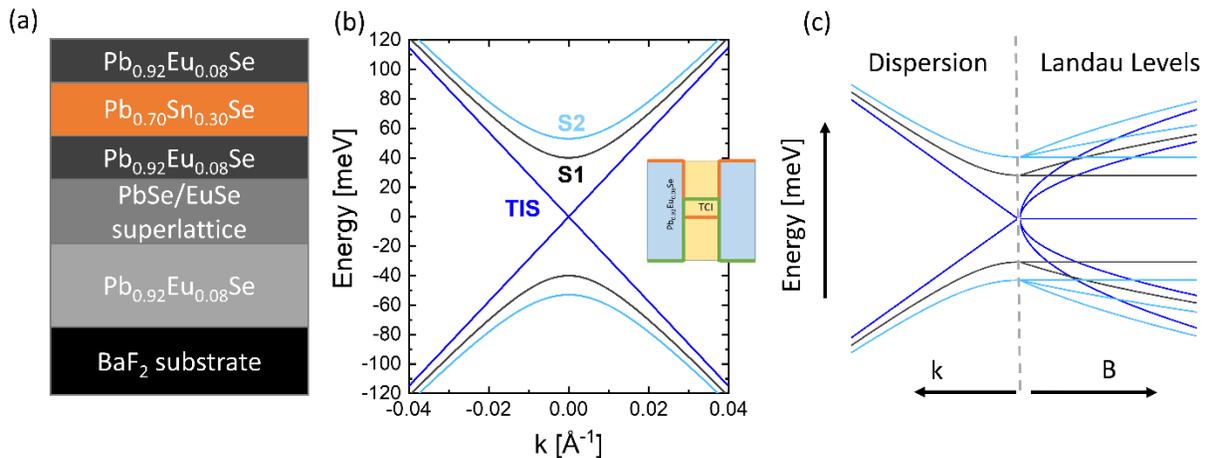
Fig. 1 (a) Structure of the quantum well. The well thickness is 50nm and barrier thickness is 40nm. (b) Band dispersion of TIS and "bulk" subbands S1 and S2. The inset diagram shows the inverted band structure of the quantum well. (c) Landau levels of each band. Spin splitting is not included in this plot.

The sample structure is shown in Fig. 1(a). A 1μm $Pb_{0.92}Eu_{0.08}Se$ layer and a PbSe/EuSe superlattice with a total thickness equal to 500nm are grown as buffer layers on the BaF_2 [111] substrate. Then, the $Pb_{0.7}Sn_{0.3}Se$ quantum well is grown between a 40nm $Pb_{0.92}Eu_{0.08}Se$ bottom barrier and a 50nm $Pb_{0.92}Eu_{0.08}Se$ top barrier. A Sn content of x=0.3 is chosen to realize an inverted bulk gap close to 100meV and an isotropic bulk Fermi surface [11]. Under the latter condition, the four Dirac surface states of the material become isotropic and identical, thus

removing the ambiguity related to valley degeneracy. [11,14] The well is encanpsulated between two identical Pb$_{0.92}$Eu$_{0.08}$Se barriers, which limit top-bottom asymmetry. The Sn concentration, layer thickness and strain characteristics are characterized by X-ray diffraction (XRD) and transmission electron microscopy (TEM), shown in our previous work [13]. Here we will focus our analysis on a single 50 nm quantum well (S1).

The inverted band structure will lead to an evanescent gapless state at the interface that are topological protected, together with gapped subbands originating from the quantum confinement of bulk states, as shown in Fig. 1(b). Each band has a separate Landau level (LL) fan illustrated in Fig. 1(c) in the presence of a magnetic field along the growth axis. The gaps, band dispersions and LLs for each subband including the topological interface states (TIS) can be derived by combining the k·p model for IV-VI semiconductors and the envelope function approach, as shown in the ref [11,13,22,23] and the appendix. Here, a far-band correction, which consists in an orbital component and spin component is expressed as $\hbar\widetilde{\omega}$. Its origin is discussed in detail in the appendix, following a similar treatment previously carried out for the bulk band structure [7,24], The LLs in the conduction (written as E) and valence band (written as H) are expressed as:

$$E_i^{N,(\uparrow,\downarrow)} = \pm\hbar\widetilde{\omega}_{eff} + \sqrt{\left(\Delta_i - N\hbar\widetilde{\omega}_{eff}\right)^2 + 2e\hbar Nv_c^2 B}$$

(1)

$$H_i^{N,(\uparrow,\downarrow)} = \pm\hbar\widetilde{\omega}_{eff} - \sqrt{\left(\Delta_i - N\hbar\widetilde{\omega}_{eff}\right)^2 + 2e\hbar Nv_c^2 B}$$

Where Δ_i is the band edge position of each subband, i is the subband index ($i = 0$ and $\Delta_0 \rightarrow 0meV$ for TIS), N denotes the LL index redefined according to ref. [10,25] (for detail see appendix B), v_c is band velocity related to the k.p interband matrix element, $\widetilde{\omega}_{eff} = \frac{eB}{\widetilde{m}_{eff}}$ represents the far band contributions to the effective mass $\widetilde{m}_{eff}$. Its meaning and origin are discussed in detail in the appendix C. This contribution gives a small parabolic correction to the linear dispersion of the interface states. We are also using the approximation that $\tilde{g}_{eff}\mu_B B \approx -\hbar\widetilde{\omega}_{eff}$, which has been used in previous works [7,24,26,27], where $\tilde{g}_{eff}$ is the far-band correction to the g-factor. Although such an approximation was originally used for bulk states [7], we show that it applies to surface states as well in the appendix C. Regardless of the accuracy of this assumption, the far-band orbital and spin Zeeman parts cannot be easily distinguished using measurements in the geometry that we have chosen in this work. Our objective will be to determine their overall impact on the Landau levels, essentially consisting in a pseudo-spin splitting. Notice here that only the far-band correction to the g-factor appears in the expression for the Landau levels. We discuss in detail later, how it relates to the total g factor. In what comes next, we determine the experimental values of Δ_i, v_c and $\widetilde{m}_{eff}$ by combining magnetooptical and magnetotransport measurements.

B. Magneto-optical Landau level spectroscopy of the band structure of topological states
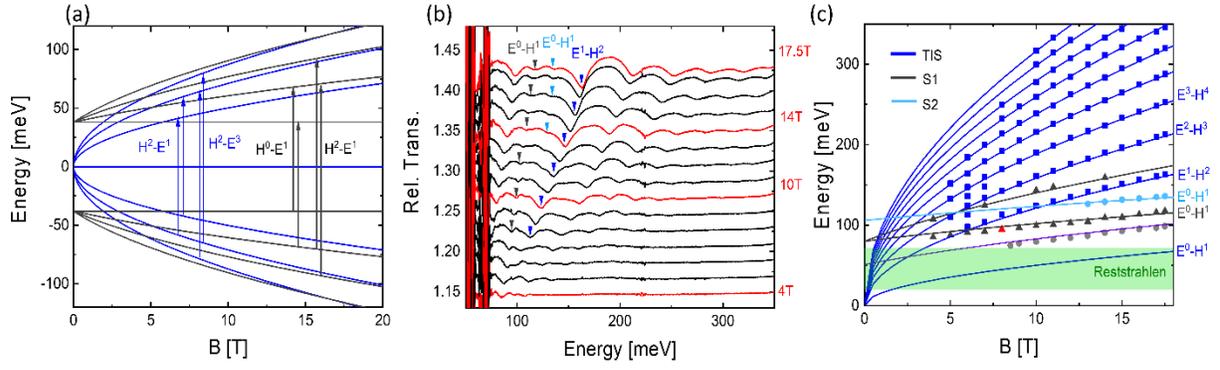
Fig. 2 (a) Landau levels of TIS and S1. Arrows represent electron transitions between LLs of the same band. For holes the transition will be from E to H. To make the transition clearer to understand, the Zeeman splitting term ($\pm\hbar\widetilde{\omega}_{eff}$) is not included in the plot. (b) Relative magneto-optical spectra (T(B)/T(0)) on S1 between 4T and 17.5T, measured at 5.5K. Special transitions are marked with different color that is consistent with Fig. 2c. (c) Fan chart extracted from spectra. All points represent the minima in fig. 2a and lines are fitting using Eq. 2. In the green region below ~70meV, the signal is blocked due to the reststrahlen band of BaF_2 and absorption through a ZnSe window used in the experiment.

We have performed magnetooptical infrared spectroscopy to extract the band parameters that appear in Eq. (1), at 5.5K using an applied magnetic field up to 17.5T in the Faraday geometry. In the presence of the magnetic field, the incident infrared electromagnetic wave excites transitions between different LLs, given dipole selection rules that conserve pseudo-spin and obey parity rules (transitions between N and N±1), as shown in Fig. 2(a). Arrows represent transitions between LLs originating from either the TIS or S1 band. According to the selection rules, the optically active interband transitions occur between H_i^N and $E_i^{N\pm1}$ Landau levels for electrons with same spin [28–31]. From Eq. 1 we can derive:

$$\Delta E = E_i^{N\pm1} - H_i^N$$
$$= \sqrt{\left[\Delta_i - (N \pm 1)\hbar\widetilde{\omega}_{eff}\right]^2 + 2e\hbar Nv_c^2 B} + \sqrt{\left(\Delta_i - N\hbar\widetilde{\omega}_{eff}\right)^2 + 2e\hbar Nv_c^2 B} \quad (2)$$

The experimental relative transmission spectra T(B)/T(0) at each field are shown in Fig. 2(b). The minima in the relative spectra, which shift to a higher energy as the field increases, represent the transition between LLs. In Fig. 2(c) the energy of each minimum is plotted versus magnetic field as points. We identify the origin of these transmission minima by fitting with Eq. 2. Transitions from same subband are in the same color. The deep blue lines represent transitions from the LLs of the TIS, the grey and light blue lines represent transitions from S1, and S2 respectively. An additional purple line represents hybrid inter-sub-band transitions of $H_0^0 - E_0^2$. A detailed discussion of this transition is beyond the scope of this work. From the fit, we can get an estimation of the band parameters including the band gap 2Δ, the band velocity v_c related to the k.p matrix element and the far-band effective mass correction $\widetilde{m}_{eff}$. A sufficient number of

points from lower-index LL transitions gives a precise fit and a precise value of the band gap Δ_i. The fitting result matches well with experimental data, for the parameters shown in table 1.

The far-band correction to the effective mass cannot however be extracted reliably by this method, as it does not influence the LL-transitions dramatically. We will show next that by combining the results of our magnetooptical Landau level spectroscopy with Shubnikov-de Haas measurements, this precision can be dramatically improved.

Table 1. Fitting parameters of sample S1 from transmission spectra. m_e is the free electron mass.

	TIS	S1	S2
Δ_i from experiment (meV)	0(+5)	40($\pm$3)	53($\pm$5)
Δ_i from calculations (meV)	0	38	49
v_c	$(4.36 \pm 0.10) \times 10^5 \ m/s$		
$|\widetilde{m}_{eff}|/m_e$	0.30($\pm$0.15)		

C. Spin splitting from Shubnikov-de-Haas measurements
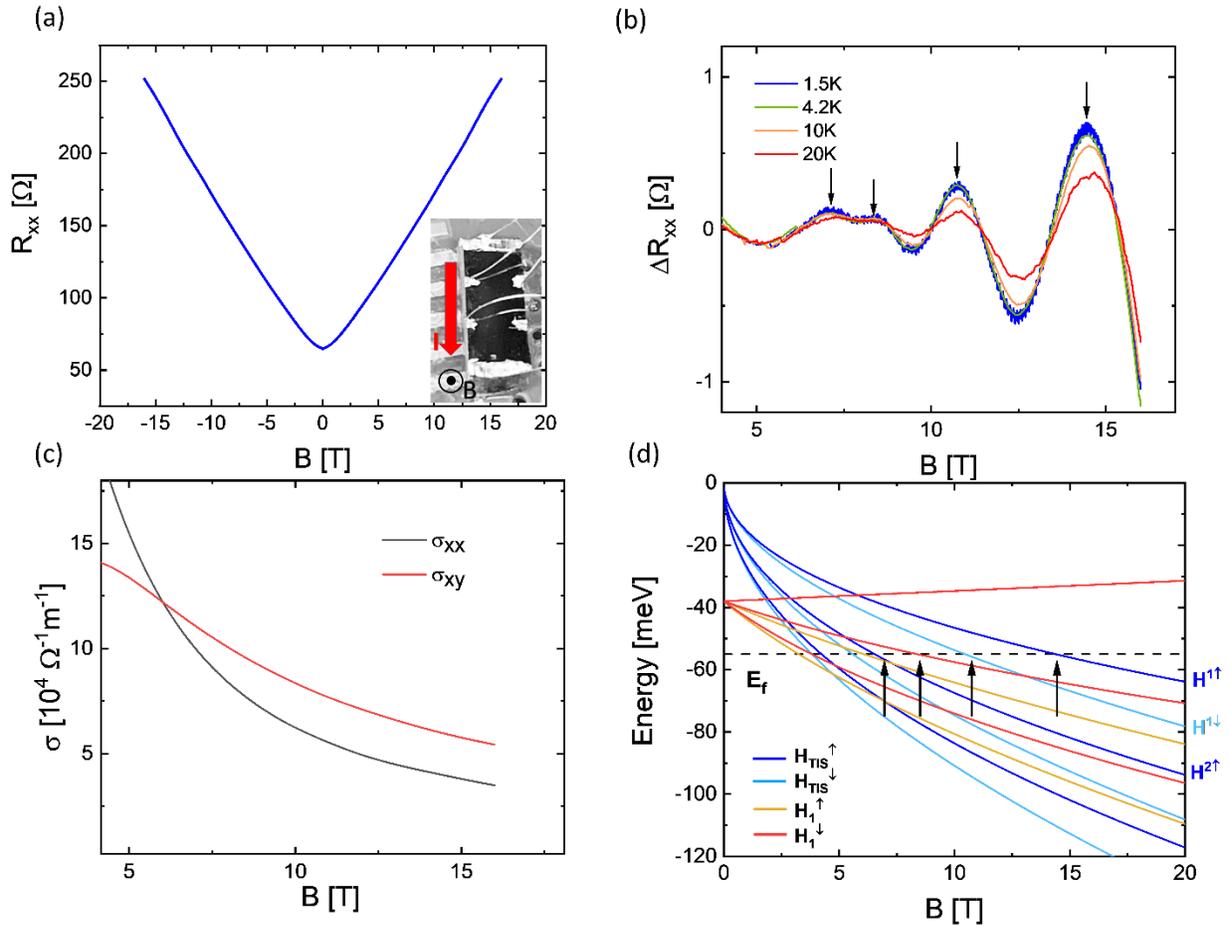
FIG 3. Transport measurement of S1. (a) R_{xx} measured at 1.5K. Weak oscillations can be observed at high field. Inset: photograph of the sample setup for transport. (b) ΔR_{xx} extracted by a linear fit. The peaks of the oscillations are indicated by black arrows. (c) Longitudinal and transverse conductance σ_{xx}, σ_{xy} calculated from Drude model. (d) Landau levels of TIS and S1. Black arrows are in the same position with (b).

Electrical magnetotransport measurements are performed between 1.5K and 20K using the standard 5-probe method, with magnetic field up to 16T. The result is shown in Fig. 3. Fig. 3(a) shows the longitudinal resistance R_{xx} versus magnetic field. Although R_{xx} is quasi-linear, we can observe small oscillations emerging at high magnetic field. By performing a linear fit, we extract this small change $\Delta R_{xx} = R_{xx} - R_{fit}$, as shown fig. 3b for different temperatures. The recovered signal exhibits Shubnikov-de Haas oscillations, which relate to the crossings between the Fermi level and Landau levels. At each crossing, the carriers are delocalized, leading to an increase of the conductivity σ_{xx}. However, whether $R_{xx} \sim \frac{\sigma_{xx}}{\sigma_{xx}^2 + \sigma_{xy}^2}$ behaves as a minimum or maximum when σ_{xx} is maximum depends on the scale of σ_{xx} and σ_{xy}. [32] In our case, σ_{xy} is larger when the field is above 5T, leading to a maximum of R_{xx} when σ_{xx} goes a maximum. The value of σ_{xy}, σ_{xx} is calculated by Drude model and shown in Fig. 3c.

The oscillating signal is aperiodic and yields only four oscillation maxima making it difficult to analyze without direct recourse to a fan-chart. The field at which the oscillation maxima occur are extracted and are indicated by arrows in Fig. 3d, where we also plot the LLs of the TIS, S1 and S2 (including Zeeman splitting) with parameters fitted from magneto-optics. The dashed line represents the Fermi level, which crosses the valence band. It can be estimated from where LL transition disappears. For example, the $E_0^2 - H_0^3$ disappear between 3.5~4T (Fig. 2c), meaning the H_0^3 LL just go across the Fermi level in that field range. By comparing several transitions, we can estimate the Fermi level to be -55 ± 5 meV (negative because the sample is p-type).

Discussion

The crossings deduced from Shubnikov-de Haas oscillations, and the predicted crossings from magneto-optical measurement, can be made to match well by further constraining the far band corrections related to $\widetilde{m}_{eff}/m_0$ as shown in Fig. 3(d). The two crossings at higher field are of particular importance, as they originate from spin-up and spin-down Landau levels with same index N=1. From Eq. 1 we can derive that the distance between these two crossings is:

$$\Delta\left(\frac{1}{B_{TIS,N=1}}\right) = \frac{1}{B_{TIS,N=1}^{\uparrow}} - \frac{1}{B_{TIS,N=1}^{\downarrow}} = \frac{4e\hbar E_f}{\widetilde{m}_{eff}\left(E_f^2 - \Delta^2\right)} \qquad (3)$$

Where $B_{TIS,N=1}^{\uparrow}, B_{TIS,N=1}^{\downarrow}$ are the crossings between the Fermi level and $H_0^{1,\uparrow}, H_0^{1,\downarrow}$. Thus, after finer tuning of the parameters to match all four crossings, the band edge correction to the effective mass $\widetilde{m}_{eff}$ can be more precisely derived to be $\frac{\widetilde{m}_{eff}}{m_e} = 0.32 \pm 0.02$. The uncertainty is mostly due to the uncertainty on the position of the Fermi level. It is in the range of the previous

reports on bulk epilayers of IV-VI materials [10,11,25]. The corresponding far-band g-factor is $\tilde{g}_{\text{eff}} \approx \frac{2m_e}{\tilde{m}_{eff}} = 6.2 \pm 0.1$. We highlight here that $\tilde{g}_{eff}$ is the effective far-band correction to the g-factor and not the overall effective g-factor. The splitting seen in Fig. 3(d) originates from spin-up and spin-down states that are originally Kramers' partners without magnetic field (appendix D). The breaking of time-reversal symmetry under a magnetic field, causes this splitting. The overall effective g-factor g of the system can be found by extracting the spin-splitting energy between Landau levels (with refined index) from the fan-chart in Fig. 3(d).
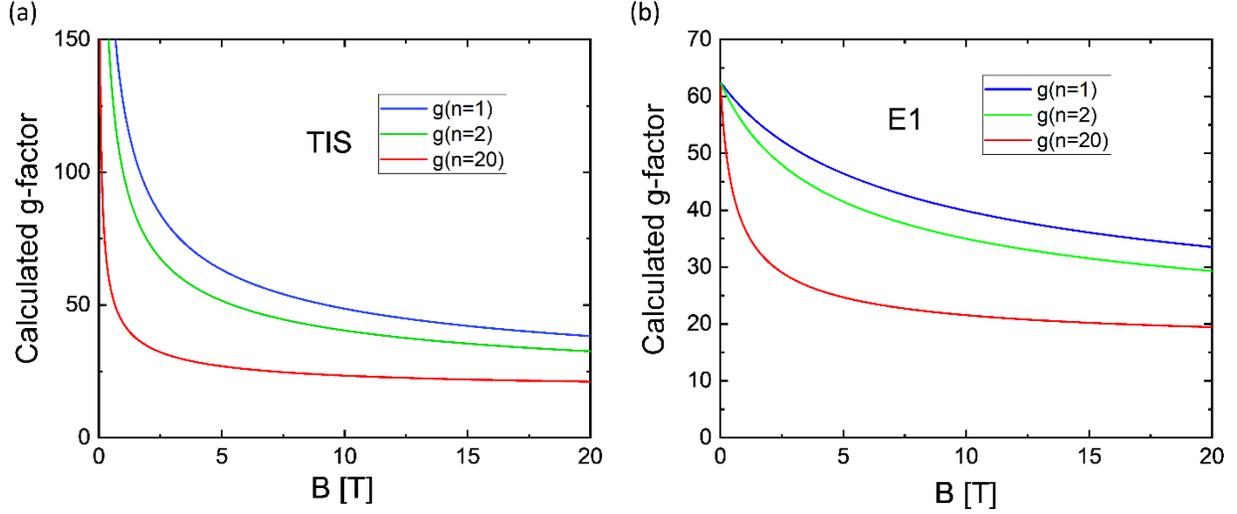
Fig. 4 Calculated effective g-factor defined in Eq. (2) for (a) topological surface states and (b) the first subband S1, which depends on the Landau index n. We choose to show the case of n=1, 2 and a large limit n=20.

The k.p treatment used above simplifies the Landau levels of TCIs by introducing an index change, explained in Appendix A. The overall effective g-factor should use the original Landau index n of Mitchell and Wallis [30] (discussed in appendix A) which describes the true spin splitting between states of identical Landau index. It is found to be consistent with spin resonance measurements in bulk [33,34], and is systematically used to characterize the spin-splitting of non-parabolic systems [14,16,35]:

$$g(n) = \frac{H(n,\uparrow) - H(n,\downarrow)}{\mu_B B} (n \geq 0) = \frac{H(N,\uparrow) - H(N+1,\downarrow)}{\mu_B B} (N \geq 0) \qquad (2)$$

It can be seen from Eq. 1 that the g is dependent on both the index N and the magnetic field B. This is not unusual for materials with non-parabolic band dispersions, and should also hold for topological surface states. The calculated result for the surface state is shown in Fig. 4a. The parameters used for calculation are taken explicitly from our magnetooptical and magnetotransport results, as discussed earlier. In a reasonable field range for measurements (2 to 20T), the g-factor for n=1 and n=2 exceeds 100 below 2T. For high-n limit, the g-factor is close to 20 between 5 and 20T.

The effective g-factor we get for the interface states is enhanced compared with reported value in bulk $Pb_{1-x}Sn_xSe$ (30~70) [14,36,37]. Such an enhancement of the surface state g-factor compared with bulk are reported in other systems, too [16,35,38]. In our case, this can be understood from the conventional Roth formula [39], where a smaller gap leads to an enhanced g. On the other hand, the calculated g-factor for the first subband S1 as shown in Fig. 4b, agrees with bulk values. The field-dependence of the g-factor can be explained by the strong mixing between orbital and spin degrees of freedom in IV-VI materials. Such behavior is also observed in other systems with strong spin-orbit coupling such as InAs [40] and HgTe [41].

In summary, we have performed magneto-optical Landau level spectroscopy and Shubnikov-de-Haas oscillation measurements on high-mobility $Pb_{0.7}Sn_{0.3}Se$ topological quantum wells. The Shubnikov-de-Haas oscillations and the magnetooptical spectra are consistent with each other. By combining the two techniques, we are able to get well-constrained band parameters including the far-band correction to the effective mass and g-factor, which is extracted from the spin splitting of Shubnikov-de-Haas peaks. The recovered effective g-factor g of the topological surface state is enhanced compared with bulk states. This effective g-factor accounts for the splitting between Landau levels of opposite spin. It is dependent on the Landau index, the magnetic field, and the energy. Finally, the existence of quantum oscillations is a promising signature to achieve the exotic quantized Hall effect predicted for the topological crystalline insulators.

Appendix A. $k \cdot p$ Hamiltonian and far-band approximation of bulk $Pb_{0.7}Sn_{0.3}Se$; Refined LL index.

A $k \cdot p$ Hamiltonian is developed by Mitchell and Wallis to describe $L_6^{\pm}$ band of lead salts. For [111] orientation in the non-trivial case, in the basis $L_{6\alpha}^+|n\rangle$, $L_{6\beta}^+|n+1\rangle$, $L_{6\alpha}^-|n\rangle$, $L_{6\beta}^-|n+1\rangle$, the Hamiltonian is written as follows:

$$\begin{pmatrix} \Delta - \left(n+\frac{1}{2}\right)\hbar\widetilde{\omega}_c + \frac{1}{2}\tilde{g}_c\mu_B B & 0 & \hbar v_z k_z & \sqrt{2(n+1)\hbar eB v_c^2} \\ 0 & \Delta - \left(n+\frac{3}{2}\right)\hbar\widetilde{\omega}_c - \frac{1}{2}\tilde{g}_c\mu_B B & \sqrt{2(n+1)n\hbar eB v_c^2} & -\hbar v_z k_z \\ \hbar v_z k_z & \sqrt{2(n+1)\hbar eB v_c^2} & -\Delta - \left(n+\frac{1}{2}\right)\hbar\widetilde{\omega}_v + \frac{1}{2}\tilde{g}_v\mu_B B & 0 \\ \sqrt{2(n+1)\hbar eB v_c^2} & -\hbar v_z k_z & 0 & -\Delta - \left(n+\frac{3}{2}\right)\hbar\widetilde{\omega}_v - \frac{1}{2}\tilde{g}_v\mu_B B \end{pmatrix}$$

Where $\widetilde{\omega}_c, \widetilde{\omega}_v, \tilde{g}_c, \tilde{g}_v$ are far-band contributions to the effective mass and g-factor, separately. n is the true Landau level index. In the non-trivial case, L_6^+ is the conduction band and L_6^- is the

valence band. α, β represent pseudo-spin direction. $L_{6\alpha}^+, L_{6\beta}^-$ represents spin-up; $L_{6\beta}^+, L_{6\alpha}^-$ represents spin-down [30,42].

Far-bands are nearly equally distant from the conduction and valence band. Thus, we can take $\widetilde{\omega}_c \approx -\widetilde{\omega}_v = \frac{eB}{\widetilde{m}}$. Similarly, $\tilde{g}_c = -\tilde{g}_v = \tilde{g}$. Previous works have shown that for bulk PbSe, $|g\mu_B B| \approx |\hbar\omega|$ within the error. Since the far-bands are close to 1eV away from the $L_6^\pm$ bulk bands, we assume the approximation will not be affected by changing Sn concentration and still holds for Pb$_{0.7}$Sn$_{0.3}$Se. Nevertheless, $\hbar\omega$ and $g\mu_B B$ always bind together to affect the energy and we cannot distinguish them by Faraday geometry.

Solving the above Hamiltonian will get the energy values for n-th Landau levels of bulk Pb$_{1-x}$Sn$_x$Se:

$$E_{L_{6\alpha}^+, L_{6\beta}^-} = \pm\hbar\widetilde{\omega} \pm \sqrt{[\Delta - (n+1)\hbar\widetilde{\omega}]^2 + 2e\hbar v_c^2(n+1)}$$

$$E_{L_{6\beta}^+, L_{6\alpha}^-} = \pm\hbar\widetilde{\omega} \pm \sqrt{[\Delta - n\hbar\widetilde{\omega}]^2 + 2e\hbar v_c^2 n}$$

Thus, we can redefine an index N such that $N = n$ for $L_{6\beta}^+$ and $N = n + 1$ for $L_{6\alpha}^+$, same applies for L_6^- bands. Such change of index is shown in Fig. 5.
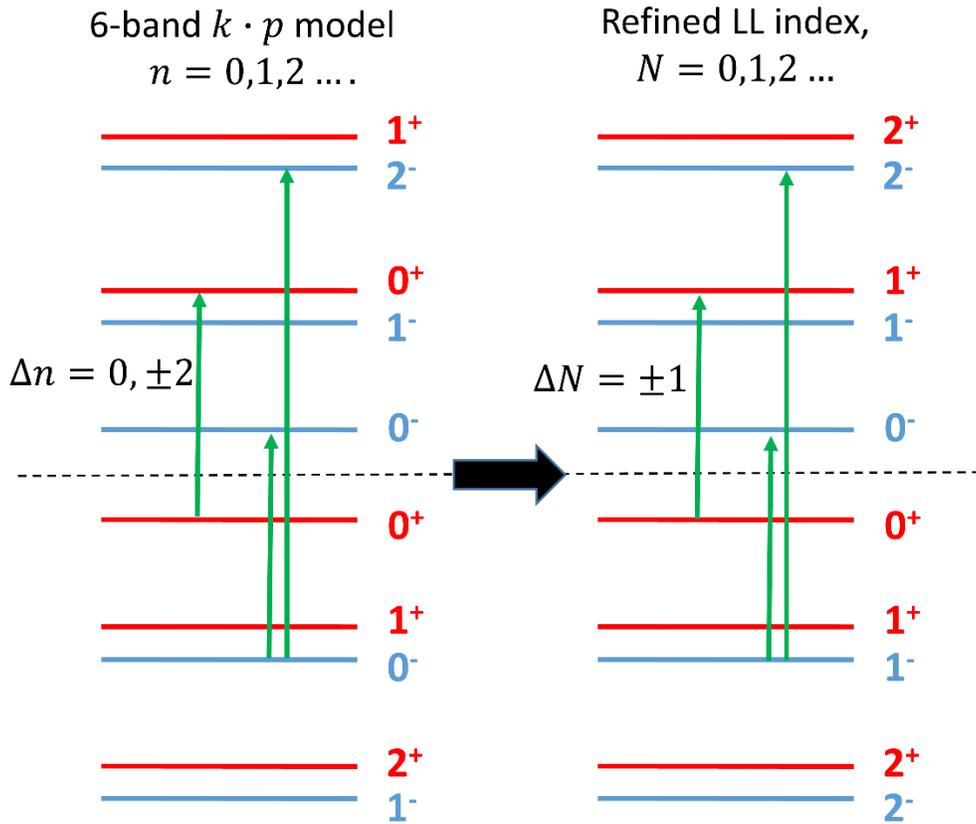
Fig. 5 Comparison between the original LL index n(left) from ref [10,30] and the refined LL index N(right) used in here and refs [7,11,24]. Green arrow represents interband transitions allowed by selection rules. For refined LL index, the transition happens between $\Delta N = \pm 1$ with same spin direction.

The selection rules for interband transitions has been discussed [28,29,31] and obey $\Delta n = 0$ or $\Delta n = \pm 2$ with same spin. In the refined N case, this is converted to $\Delta N = \pm 1$ with same spin direction. Transitions are plotted as green arrows in Fig.5.

Appendix B. $k \cdot p$ Envelope function model for single quantum well

The $k \cdot p$ model can be further applied to the quantum wells, which is already discussed in previous works [11,13,43]. We will briefly discuss here for the reference.
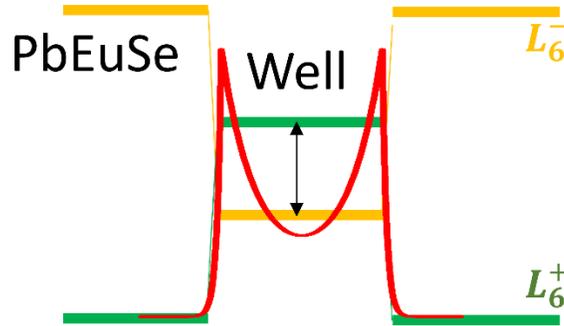
Fig. 6 Band diagram of the quantum well.

The 4-band k.p Hamiltonian describing the electronic structure of IV-VI quantum wells in the basis $|L_6^+, \uparrow\rangle, |L_6^+, \downarrow\rangle, |L_6^-, \uparrow\rangle, |L_6^-, \downarrow\rangle$ is written as follows:

$$\widehat{H} = \begin{pmatrix} V_-(z) & 0 & -i\hbar v_z \partial_z & 0 \\ 0 & V_-(z) & 0 & i\hbar v_z \partial_z \\ -i\hbar v_z \partial_z & 0 & -2|\Delta| + V_+(z) & 0 \\ 0 & i\hbar v_z \partial_z & 0 & -2|\Delta| + V_+(z) \end{pmatrix}$$

Here, V_+ represents the band offset at the interfaces (z=0 and z=L). $V_\pm(z) = \pm V$ outside the well and 0 inside it (V is much larger than 2Δ). $-2|\Delta|$ is the position of the valence band edge, with the conduction band edge in the well taken to be at 0.

The detailed solution using envelope functions can be referred to the references above. The result for $-2\Delta < E < 0$ is

$$\tanh\left(\frac{\kappa d}{2}\right) = -\frac{\rho(E + 2\Delta)}{\kappa(E + 2\Delta - V)}, \quad even \ case$$

$$\coth\left(\frac{\kappa d}{2}\right) = -\frac{\rho(E + 2\Delta)}{\kappa(E + 2\Delta - V)}, \quad odd \ case$$

Here $\kappa = -\frac{1}{\hbar v_z}\sqrt{-E(E + 2|\Delta|)}$. For the sample S1, $d = 50nm$, $2\Delta = 100meV$ (gap of bulk Pb$_{0.70}$Sn$_{0.30}$Se) $v_z = 4.36E5\ m/s$. And we take the gap of Pb$_{0.92}$Eu$_{0.08}$Se to be $V = 250meV$. [44] We can calculate the gap of TIS, S1 and S2 shown in table 1.

Appendix C. Spin-Splitting of the topological surface state

Landau levels can be numerically solved by introducing perturbation Hamiltonian

$$H_{mn}^{eff}(B) = \int_{-\infty}^{\infty} dz \langle \overline{\Psi}_m | \Delta H | \overline{\Psi}_n \rangle$$

Where

$$\Delta H = \begin{pmatrix} -(N-1)\hbar\widetilde{\omega}_c & 0 & 0 & \sqrt{2e\hbar v_c^2 BN} \\ 0 & -(N+1)\hbar\widetilde{\omega}_c & \sqrt{2e\hbar v_c^2 BN} & 0 \\ 0 & \sqrt{2e\hbar v_c^2 BN} & -(N-1)\hbar\widetilde{\omega}_v & 0 \\ \sqrt{2e\hbar v_c^2 BN} & 0 & 0 & -(N+1)\hbar\widetilde{\omega}_v \end{pmatrix}$$

Here we already take the approximation $\tilde{g}_{c,v}\mu_B B \approx \hbar\widetilde{\omega}_{c,v}$. For the TSS state, the wavefunction in Eq. S1 is mixed, which means $|F_1^{TSS}|^2 = |F_2^{TSS}|^2$. The effective Hamiltonian then becomes $H_{ii}^{eff}(B) = \int_{-\infty}^{\infty} dz \langle \overline{\Psi}_i | \Delta H | \overline{\Psi}_i \rangle = -(N \pm 1)\hbar(\widetilde{\omega}_c + \widetilde{\omega}_v)/2$. In bulk, previous work has treated $|\widetilde{\omega}_c| \approx |\widetilde{\omega}_v|$. If we set them equal to each, the far band corrections for the TSS will be zero. We thus define $\widetilde{\omega}_{eff} = \frac{\widetilde{\omega}_c + \widetilde{\omega}_v}{2}$ and $\tilde{g}_{eff}\mu_B B \approx \hbar\widetilde{\omega}_{eff}$. These terms require electron-hole asymmetry to be finite. The corresponding $H^{eff}(B)$ describing surface states then looks like the bulk one [45]. In practice, we find that the result is well described by the empirical equation:

$$E_i^{N,(\uparrow,\downarrow)} = \pm\hbar\widetilde{\omega}_{eff} \pm \sqrt{\left(\Delta_i - N\hbar\widetilde{\omega}_{eff}\right)^2 + 2e\hbar N v_c^2 B}$$

$$\widetilde{\omega}_{eff} = \frac{eB}{\widetilde{m}_{eff}}$$

$\widetilde{m}_{eff}$ can be estimated theoretically, by taking $\widetilde{m}_c = 0.23 \pm 0.06 m_0$, $\widetilde{m}_v = -0.115 \pm 0.03$ from Bauer [10]. We find $|\widetilde{m}_{eff}| = 0.23 \pm 0.19$. Our own measurement of $|\widetilde{m}_{eff}|$ falls in this range, as shown in the main text.

Appendix D. Origin of the spin-split

In this section we would like to relate our result to the common model used in TIs. Following the discussion in appendix B, C we can get the eigenstates $|\psi_{c,\uparrow}\rangle, |\psi_{c,\downarrow}\rangle, |\psi_{v,\uparrow}\rangle, |\psi_{v,\downarrow}\rangle$, which represent spin-up or spin-down eigenstates in conduction/valence bands. They can be re-written as the symmetric and antisymmetric linear combination of states on the top $|\psi_t \uparrow\rangle, |\psi_t \downarrow\rangle$ and bottom

$|\psi_b \uparrow\rangle, |\psi_b \downarrow\rangle$ surface. If we change the basis back, eg. $|\psi_{t,b} \uparrow\rangle = (|\psi_{c,\uparrow}\rangle \pm |\psi_{v,\uparrow}\rangle)/\sqrt{2}$, $|\psi_{t,b} \downarrow\rangle = (|\psi_{c,\downarrow}\rangle \pm |\psi_{v,\downarrow}\rangle)/\sqrt{2}$, the effective Hamiltonian is

$$H = \begin{pmatrix} 0 & \sqrt{2e\hbar v_c^2 BN} & -(N-1)\hbar\widetilde{\omega} & 0 \\ \sqrt{2e\hbar v_c^2 BN} & 0 & 0 & -(N+1)\hbar\widetilde{\omega} \\ -(N-1)\hbar\widetilde{\omega} & 0 & 0 & -\sqrt{2e\hbar v_c^2 BN} \\ 0 & -(N+1)\hbar\widetilde{\omega} & -\sqrt{2e\hbar v_c^2 BN} & 0 \end{pmatrix}$$

The Hamiltonian has similar form as the Hamiltonian of four Dirac-type surface state [46,47]. The square root term comes from performing ladder operator to the $\hbar v k_\pm$ term. The eigenenergy is solved to be

$$E(N) = \pm\hbar\widetilde{\omega} \pm \sqrt{\hbar^2\widetilde{\omega}^2 N^2 + 2e\hbar v_c^2 BN}$$

When field is zero, the states from top and bottom surface are Kramers' partnerss. [15]
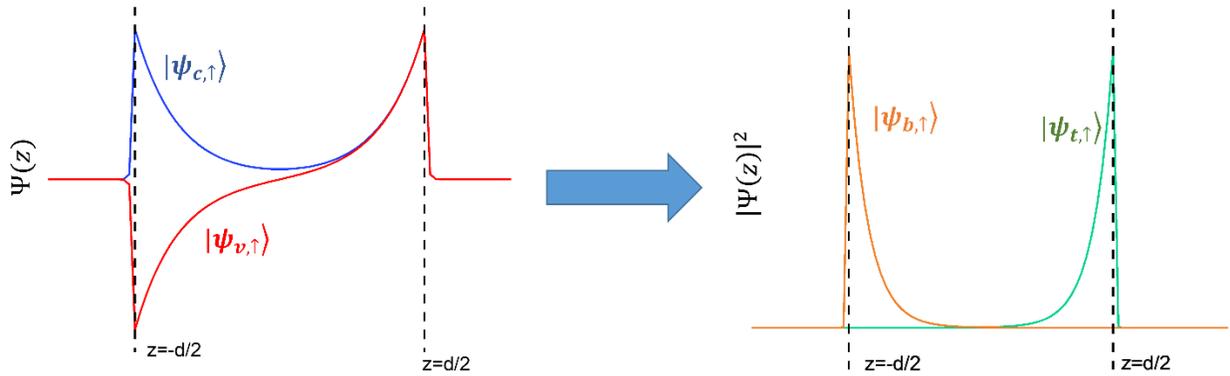
Fig.7 A sketch showing the parity and probability distribution of different states. (Left) The wavefunction of $|\psi_{c,\uparrow}\rangle$, $|\psi_{v,\uparrow}\rangle$ along z direction. To show they have opposite parity we are not plotting $|\Psi(z)|^2$. (Right) Probability distribution of new basis $|\psi_t \uparrow\rangle$, $|\psi_b \uparrow\rangle$.

In our original basis, $|\psi_{c,\uparrow}\rangle$, $|\psi_{v,\uparrow}\rangle$ have opposite parity. Their symmetric and anti-symmetric combination naturally lead to $|\psi_t \uparrow\rangle$, $|\psi_b \uparrow\rangle$ that lie on separate surface, as shown in Fig. 7. As field goes up, these states get mixed because of the $-(N \pm 1)\hbar\widetilde{\omega}$ term in the Hamiltonian. As a result the mixed basis $|\psi_{c,\uparrow\downarrow}\rangle$, $|\psi_{v,\uparrow\downarrow}\rangle$ is more commonly used.

References

[1]   L. Fu, *Topological Crystalline Insulators*, Phys. Rev. Lett. **106**, 106802 (2011).

[2]   T. H. Hsieh, H. Lin, J. Liu, W. Duan, A. Bansil, and L. Fu, *Topological Crystalline Insulators in the SnTe Material Class*, Nat. Commun. **3**, 982 (2012).

[3]   P. Dziawa, B. J. Kowalski, K. Dybko, R. Buczko, A. Szczerbakow, M. Szot, E. Łusakowska, T. Balasubramanian, B. M. Wojek, M. H. Berntsen, O. Tjernberg and T. Story, *Topological Crystalline Insulator States in Pb$_{1-x}$Sn$_x$Se*, Nat. Mater. **11**, 1023 (2012).

[4]   X. Li, F. Zhang, and A. H. MacDonald, *SU (3) Quantum Hall Ferromagnetism in SnTe*, Phys. Rev. Lett. **116**, 026803 (2016).

[5]   C. Fang, M. J. Gilbert, and B. A. Bernevig, *Large-Chern-Number Quantum Anomalous Hall Effect in Thin-Film Topological Crystalline Insulators*, Phys. Rev. Lett. **112**, 046801 (2014).

[6]   I. Sodemann, Z. Zhu, and L. Fu, *Quantum Hall Ferroelectrics and Nematics in Multivalley Systems*, Phys. Rev. X **7**, 041068 (2017).

[7]   B. A. Assaf, T. Phuphachong, E. Kampert, V. V. Volobuev, P. S. Mandal, J. Sánchez-Barriga, O. Rader, G. Bauer, G. Springholz, L. A. de Vaulchier, and Y. Guldner, *Negative Longitudinal Magnetoresistance from the Anomalous N=0 Landau Level in Topological Materials.*, Phys. Rev. Lett. **119**, 106602 (2017).

[8]   C. Zhang, Y. Liu, X. Yuan, W. Wang, S. Liang, and F. Xiu, *Highly Tunable Berry Phase and Ambipolar Field Effect in Topological Crystalline Insulator Pb$_{1-x}$Sn$_x$Se*, Nano. Lett. **15**, 2161 (2015).

[9]   Alexander Kazakov, Wojciech Brzezicki, Timo Hyart, Bartłomiej Turowski, Jakub Polaczyński, Zbigniew Adamus, Marta Aleszkiewicz, Tomasz Wojciechowski, Jaroslaw Z. Domagala, Ondřej Caha, Andrei Varykhalov, Gunther Springholz, Tomasz Wojtowicz, Valentine V. Volobuev, and Tomasz Dietl, *Signatures of Dephasing by Mirror-Symmetry Breaking in Weak-Antilocalization Magnetoresistance across the Topological Transition in Pb$_{1-x}$Sn$_x$Se*, Phys. Rev. B **103**, 245307 (2021).

[10]   G. Bauer, *Magnetooptical Properties of IV–VI Compounds*, Narrow Gap Semiconductors Physics and Applications, Vol. 133 (Springer Berlin Heidelberg, Berlin, Heidelberg, Heidelberg, 1980), pp. 427–446.

[11]   G. Krizman, B. A. Assaf, T. Phuphachong, G. Bauer, G. Springholz, L. A. de Vaulchier, and Y. Guldner, *Dirac Parameters and Topological Phase Diagram of Pb$_{1-x}$Sn$_x$Se from Magnetospectroscopy*, Phys. Rev. B **98**, 245202 (2018).

[12]   C. M. Polley, V. Jovic, T.-Y. Su, M. Saghir, D. Newby, Jr., B. J. Kowalski, R. Jakiela, A. Barcz, M. Guziewicz, T. Balasubramanian, G. Balakrishnan, J. Laverock, and K. E. Smith, *Observation of Surface States on Heavily Indium-Doped SnTe(111), a Superconducting Topological Crystalline Insulator*, Phys. Rev. B **93**, 075132 (2016).

[13]   Jiashu Wang, X. Liu, C. Bunker, L. Riney, B. Qing, S. K. Bac, M. Zhukovskyi, T. Orlova, S. Rouvimov, M. Dobrowolska, J. K. Furdyna, and B. A. Assaf, *Weak Antilocalization beyond the Fully Diffusive Regime in Pb$_{1-x}$Sn$_x$Se Topological Quantum Wells*, Phys. Rev. B **102**, 155307 (2020).

[14]   J. Melngailis, T. C. Harman, and W. C. Kernan, *Shubnikov-de Haas Measurements in Pb$_{1-x}$Sn$_x$Se*, Phys. Rev. B **5**, 2250 (1972).

[15] Y.-S. Fu, T. Hanaguri, K. Igarashi, M. Kawamura, M. S. Bahramy, and T. Sasagawa, *Observation of Zeeman Effect in Topological Surface State with Distinct Material Dependence*, Nat. Commun. **7**, 10829 (2016).

[16] Z. Zhang, W. Wei, F. Yang, Z. Zhu, M. Guo, Y. Feng, D. Yu, M. Yao, N. Harrison, R. McDonald, Y. Zhang, D. Guan, D. Qian, J. Jia, and Y. Wang, *Zeeman Effect of the Topological Surface States Revealed by Quantum Oscillations up to 91 Tesla*, Phys. Rev. B **92**, 235402 (2015).

[17] A. A. Taskin and Y. Ando, *Berry Phase of Nonideal Dirac Fermions in Topological Insulators*, Phys. Rev. B **84**, 035301 (2011).

[18] J. Xiong, Y. Luo, Y. Khoo, S. Jia, R. J. Cava, and N. P. Ong, *High-Field Shubnikov–de Haas Oscillations in the Topological Insulator Bi_2Te_2Se*, Phys. Rev. B **86**, 045314 (2012).

[19] J. G. Analytis, R. D. McDonald, S. C. Riggs, J.-H. Chu, G. S. Boebinger, and I. R. Fisher, *Two-Dimensional Surface State in the Quantum Limit of a Topological Insulator*, Nat. Phys. **6**, 960 (2010).

[20] R. Winkler, *Spin-Orbit Coupling Effects in Two-Dimensional Electron and Hole Systems* (Springer Berlin Heidelberg, 2003).

[21] T. H. Hsieh, H. Lin, J. Liu, W. Duan, A. Bansil, and L. Fu, *Topological Crystalline Insulators in the SnTe Material Class*, Nat. Commun. **3**, 982 (2012).

[22] G. Krizman, B. A. Assaf, G. Bauer, G. Springholz, L. A. de Vaulchier, and Y. Guldner, *Miniband Engineering and Topological Phase Transitions in Topological-Insulator–Normal-Insulator Superlattices*, Phys. Rev. B **103**, 235302 (2021).

[23] G. Bastard, *Wave Mechanics Applied to Semiconductor Heterostructures* (Wiley-Interscience, 1991).

[24] T. Phuphachong, B. Assaf, V. Volobuev, G. Bauer, G. Springholz, L.-A. de Vaulchier, and Y. Guldner, *Dirac Landau Level Spectroscopy in $Pb_{1-x}Sn_xSe$ and $Pb_{1-x}Sn_xTe$ across the Topological Phase Transition: A Review*, Crystals (Basel) **7**, 29 (2017).

[25] G. Bauer, H. Pascher, and W. Zawadzki, *Magneto-Optical Properties of Semimagnetic Lead Chalcogenides*, Semicond. Sci. Technol. **7**, 703 (1992).

[26] G. Krizman, B. A. Assaf, T. Phuphachong, G. Bauer, G. Springholz, G. Bastard, R. Ferreira, L. A. de Vaulchier, and Y. Guldner, *Tunable Dirac Interface States in Topological Superlattices*, Phys. Rev. B **98**, 075303 (2018).

[27] H. Pascher, G. Bauer, and R. Grisar, *Magnetooptical Investigations and Four-Wave-Mixing Spectroscopy of PbSe*, Phys. Rev. B **38**, 3383 (1988).

[28] G. Krizman, B. A. Assaf, M. Orlita, T. Phuphachong, G. Bauer, G. Springholz, G. Bastard, R. Ferreira, L. A. de Vaulchier, and Y. Guldner, *Avoided Level Crossing at the Magnetic Field Induced Topological Phase Transition Due to Spin-Orbital Mixing*, Phys. Rev. B **98**, 161202 (2018).

[29] H. Burkhard, G. Bauer, and W. Zawadzki, *Band-Population Effects and Intraband Magneto-Optical Properties of a Many-Valley Semiconductor: PbTe*, Phys. Rev. B **19**, 5149 (1979).

[30] D. L. Mitchell and R. F. Wallis, *Theoretical Energy-Band Parameters for the Lead Salts*, Physical Review **151**, 581 (1966).

[31] B. A. Assaf, T. Phuphachong, V. V. Volobuev, G. Bauer, G. Springholz, L.-A. de Vaulchier, and Y. Guldner, *Magnetooptical Determination of a Topological Index*, NPJ Quantum Material **2**, 26 (2017).

[32] N. Miura, *Physics of Semiconductors in High Magnetic Fields* (Oxford University Press, 2007).

[33] M. S. Adler, C. R. Hewes, and S. D. Senturia, *K·p Model for the Magnetic Energy Levels in PbTe and $Pb_{1-x}Sn_xTe$*, Phys. Rev. B **7**, 5186 (1973).

[34] C. K. N. Patel and R. E. Slusher, *Electron Spin-Flip Raman Scattering in PbTe*, Physical Review **177**, 1200 (1969).

[35] Y. Jiang, M. Ermolaev, G. Kipshidze, S. Moon, M. Ozerov, D. Smirnov, Z. Jiang, and S. Suchalkin, *Giant G-Factors and Fully Spin-Polarized States in Metamorphic Short-Period InAsSb/InSb Superlattices*, Nat. Commun. **13**, 5960 (2022).

[36] A. R. Calawa, J. O. Dimmock, T. C. Harman, and I. Melngailis, *Magnetic Field Dependence of Laser Emission in $Pb_{1-x}Sn_xSe$ Diodes*, Phys. Rev. Lett. **23**, 7 (1969).

[37] P. Kästner and G. Landwehr, *Determination of the Transverse G-Factors for n- and p-Type PbSe by Magnetoacoustic Quantum Oscillations*, Physica Status Solidi (b) **41**, K71 (1970).

[38] R. Xiao, J. Zhang, J. Chamorro, J. Kim, T. M. McQueen, D. Vanderbilt, M. Kayyalha, Y. Li, and N. Samarth, *Integer Quantum Hall Effect and Enhanced g Factor in Quantum-Confined Cd_3As_2 Films*, Phys. Rev. B **106**, L201101 (2022).

[39] L. M. Roth, B. Lax, and S. Zwerdling, *Theory of Optical Magneto-Absorption Effects in Semiconductors*, Physical Review **114**, 90 (1959).

[40] J. Yuan, M. Hatefipour, B. A. Magill, W. Mayer, M. C. Dartiailh, K. Sardashti, K. S. Wickramasinghe, G. A. Khodaparast, Y. H. Matsuda, Y. Kohama, Z. Yang, S. Thapa, C. J. Stanton, and J. Shabani, *Experimental Measurements of Effective Mass in Near-Surface InAs Quantum Wells*, Phys. Rev. B **101**, 205310 (2020).

[41] X. C. Zhang, K. Ortner, A. Pfeuffer-Jeschke, C. R. Becker, and G. Landwehr, *Effective g Factor of N-Type $HgTe/Hg_{1-x}Cd_xTe$ Single Quantum Wells*, Phys. Rev. B **69**, 115340 (2004).

[42] R. L. Bernick and L. Kleinman, *Energy Bands, Effective Masses and g-Factors of the Lead Salts and SnTe*, Solid State Commun. **8**, 569 (1970).

[43] J. Wang, T. Wang, M. Ozerov, Z. Zhang, S.-K. Bac, H. Trinh, M. Zhukovskyi, T. Orlova, H. Ambaye, J. Keum, D. Smirnov, V. Lauter, X. Liu, B. A. Assaf, *Magnetic Proximity-Induced Energy Gap of Topological Surface States*, arXiv:2207.07685 (2022).

[44] M. Simma, G. Bauer, and G. Springholz, *Temperature Dependent Band Offsets in PbSe/PbEuSe Quantum Well Heterostructures*, Appl. Phys. Lett. **101**, 172106 (2012).

[45]   G. Krizman, *Étude Magnéto-Optique Des Transitions de Phase Topologique Dans Les Alliages Pb$_{1-x}$Sn$_x$Se et Leurs Hétérostructures*, Université Paris sciences et lettres, 2020.

[46]   R. Yu, W. Zhang, H. J. Zhang, S. C. Zhang, X. Dai, and Z. Fang, *Quantized Anomalous Hall Effect in Magnetic Topological Insulators*, Science **329**, 61 (2010).

[47]   X. L. Qi and S. C. Zhang, *Topological Insulators and Superconductors*, Rev. Mod. Phys. **83**, 1057 (2011).